

Tetrode technology: advances in implantable hardware, neuroimaging, and data analysis techniques

M.S. Jog^a, C.I. Connolly^b, Y. Kubota^c, D.R. Iyengar^c, L. Garrido^d, R. Harlan^e,
A.M. Graybiel^{c,*}

^a *University of Western Ontario, London, Ont., Canada N6A 5A5*

^b *SRI International, Menlo Park, CA 94025, USA*

^c *Department of Brain and Cognitive Sciences and the McGovern Institute for Brain Research, M.I.T., Cambridge, MA 02139, USA*

^d *MRI Unit, Charlestown MRI Facility, MGH, Charlestown, MA 02129, USA*

^e *Specialty Machining, Wayland, MA 01778, USA*

Received 4 September 2001; received in revised form 1 April 2002; accepted 2 April 2002

Abstract

The technical advances in hardware and software for multiunit recordings have made it easier to gather data from a large number of neurons for behavioral correlations. This paper discusses several such advances in implantable hardware, magnetic resonance imaging of electrodes in situ, and data analysis software for multiple simultaneous signals. © 2002 Elsevier Science B.V. All rights reserved.

Keywords: Multi-channel recording; Tetrodes; Data analysis; Magnetic resonance imaging

1. Introduction

Methods for recording simultaneously from large numbers of neurons in behaving animals have opened the possibility of analyzing neuronal activity at the network level. At the same time, these methods have generated challenges in terms both of developing hardware capable of reliable multiple single-unit recording and of developing accurate and efficient methods for acquisition, unit identification and analysis of large sets of data. Among the several leading methods developed, recordings with tetrodes have major advantages in terms of the reliability of unit identification (Recce and O'Keefe, 1989; Wilson and McNaughton, 1993; Gray

et al., 1995; Harris et al., 2000; Henze et al., 2000). A number of software approaches for data analysis have been developed, and evidence suggests that the most reliable methods involve automatic unit identification (spike sorting) with manual verification (Harris et al., 2000). We present here hardware modifications of the Wilson-McNaughton tetrode headstage and a new analysis algorithm that features tools for rapid and reliable spike sorting.

For hardware design, our goal was to produce a lightweight, magnetic resonance imaging (MRI)-compatible, autoclavable and reusable tetrode microdrive assembly, modified from the Wilson-McNaughton headstage (Wilson and McNaughton, 1993), suitable for use in freely moving rodents even under conditions of vigorous activity. For software design, our goal was to develop a reliable, user friendly, automated cluster cutting analysis program based on estimates of signal power of each spike in a power space and ready user verification with the aid of three dimensional displays. These hardware and software improvements have been

* Corresponding author. Tel.: +1-617-253-5785; fax: +1-617-253-1599

E-mail address: graybiel@mit.edu (A.M. Graybiel).

tested in studies of the striatum in freely moving rats and mice (Jog et al., 1999; Kubota et al., 2000).

2. Hardware

2.1. Drive design and assembly

Wilson and McNaughton (1993) developed an implantable tetrode headstage with multiple microdrives made from telescoping tubes that hold a single tetrode in parallel with a threaded screw allowing independent mobility of each tetrode. We have modified this drive assembly to increase its versatility. The standard hand-made tetrode microdrives consist of steel tubing and threaded rods held together by dental acrylic. The device is fragile, relatively heavy, and is not compatible with either MRI or autoclaving procedures. We have designed a light-weight device that is precision-machined to precise specifications almost entirely from plastic and that is safe under high magnetic fields and high temperatures. As a result, MRI images can be obtained safely, and the device can be autoclaved for sterilization prior to implantation and reused for repeated implantation. Because the drive is designed on a computer-assisted design system (CAD), it can be modified easily to house anywhere from 6 to 12 or even 28 tetrodes without changing the basic structure and shape of the device. The 6-tetrode version is shown in Fig. 1. The device can be manufactured in two halves so that it readily accommodates dual-site recordings with multiple tetrodes. Because the drive is lightweight, it is particularly useful for recordings made in the awake, behaving rodent. The device retains the central strength of the original Wilson-McNaughton tetrode microdrive assembly, allowing repeated, independent mobility of each tetrode.

Each microdrive assembly has a fixed body micro-machined from Delrin and 6–12 identical microdrives (Fig. 1). The composite body has a central pole that holds the interface connector. This makes the system extremely robust. It is virtually unbreakable, unlike drives made from dental acrylic. Each microdrive then has a mobile component with a set screw and three precision-drilled holes for interfacing with the main body. The outer hole is for brass rod that adds structural stability, the middle hole holds the screw for advancing the microdrive, and the inner hole houses the telescoping tubes and the tetrode. The telescoping tubes consist of medical-grade polyimide tubes (Phelps Dodge Industries) of different sizes (inner diameters of 0.0159 in., 0.0062 in. and 0.0035 in.), which are non-magnetic and extremely smooth. Consequently, the tetrode, which is glued to the innermost tube, is not damaged while being advanced by lowering the mobile top piece by turning the screw. As the tubing is non-conductive, it could

provide additional electrical insulation and may have the benefit of reducing electrical noise picked up by tetrodes in metal tubing. In addition, the use of plastic makes the drive significantly lighter than earlier dental acrylic drives, which weighed 13–15 g. The drives weigh ca. 7 g for rat (Fig. 1A and B) (Jog et al., 1999) and 2.2 g (Fig. 1D and E; Kubota et al., 2000). The low weight is advantageous for work in freely-moving rodents (Jog et al., 1999; Kubota et al., 1999, 2000).

Individual tetrodes are inserted into the telescoping tube assembly once the drive is assembled. The free ends of the tetrodes are silver plated onto the pins of the connector and secured with heat shrink tube. The entire drive is enclosed in and protected by a transparent plastic cone with a removable cap that is screwed to the body of the drive. This cone, made from polished Lexan, is sturdy, lightweight, shatter proof, translucent and heat resistant. The ease of temporarily removing the cap post-implantation allows for repair of drive components as necessary during the course of experiments.

2.2. Tetrode manufacture and calibration

The tetrode, which is made of four twisted micro-wires, is an extracellular recording microelectrode with four closely-spaced recording tips whose relative positions are distinct in three dimensions. Simultaneous capture of each spike by these four recording channels allows superior resolution of putative neuronal sources compared to that obtainable with single-tip extracellular electrodes (Gray et al., 1995; Harris et al., 2000). The resulting increase in the number of identifiable recorded single units allows detailed investigation of inter-neuron discharge relationships and complements other methods for ensemble analysis of recorded neuronal populations (Deadwyler and Hampson, 1997; Eichenbaum and Davis, 1998). Tetrodes have been primarily used to obtain recordings in freely-behaving rodents (Wilson and McNaughton, 1993, 1994; Skaggs and McNaughton, 1996; Eichenbaum and Davis, 1998; Jog et al., 1999; Kubota et al., 1999, 2000), although technological limitations have been pointed out (Hampson and Deadwyler, 1999). The four-dimensional data acquired by tetrodes not only allow superior signal source separation, but also permit localization of putative signal generators in the tissue surrounding the tetrode (Harris et al., 2000; Henze et al., 2000). These advantages of the tetrode critically depend on the geometry of the tetrode tips and the integrity of this geometry as the tetrode is advanced through brain tissue.

Microscopic examination of ca. 100 tetrodes showed that their tips were variably and significantly splayed apart (between 20 and 30 μm) at least 70% of the time after acute cerebral penetration and 100% of the time after chronic implantation. Given that the original tip-to-tip separation is between 20 and 30 μm , this addi-

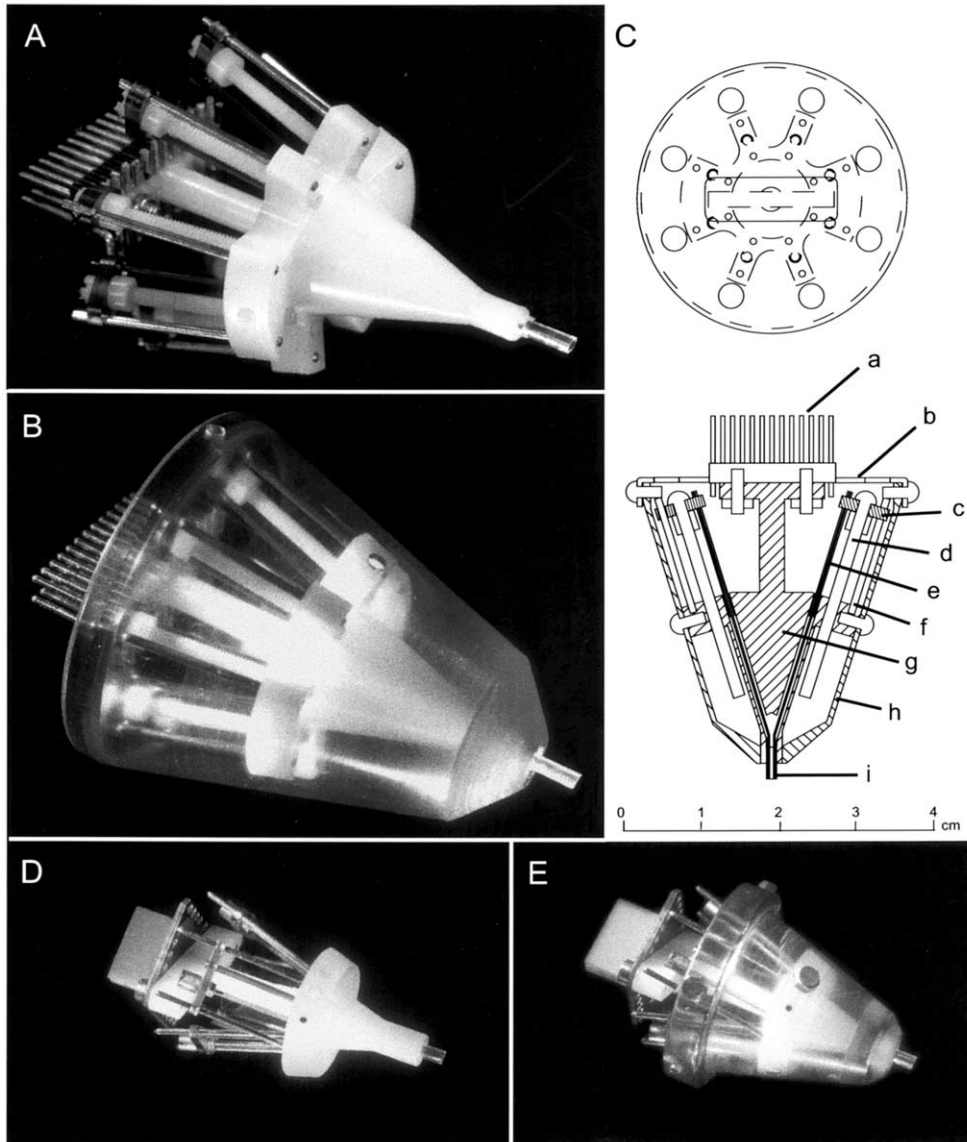


Fig. 1. Implantable headstage consisting of independently moveable microdrives. Six of eight microdrives are used to hold six tetrodes (24 channels). The photographs in A and B illustrate the internal body of the microdrive assembly (A) and the body with a protective plastic cone (B). The engineering drawing (C) shows details of the design in a top view (upper figure) and side view (lower figure). During recording, a preamplifier is connected to a 26-pin connector (a) held at the top of the Delrin body (g). The body, microdrives and tetrodes are protected by the plastic cone (h) and removable cap (b). Each tetrode is held inside polyimide telescoping tubings (e) that are glued to a mobile top piece (c). By turning the screw (d), the top piece moves along a supporting brass rod (f), and the tetrode enters into a polyimide casing (i) and then comes out of the open face of the casing and can be lowered or raised in the brain. A headstage for mouse is shown in D and E. This headstage keeps the same engineering design as the headstages for rats, but it holds four tetrodes (16 channels) and weighs 2.2 g.

tional splaying represents a large variance in the tip geometry. We therefore added a manufacturing step to improve the rigidity and integrity of the tetrode. We first followed the original procedure for folding, twisting and heat-fusing of the insulated 12 μm nickel–chromium tetrode wires to produce a composite four-channel tip (ca. 45 μm diameter) with corresponding free ends as described by Gray et al. (1995). We then dipped the entire tetrode, excluding the free ends, in biocompatible, extra-thin, cyanoacrylate glue (Pacer Technology©) for 5 s. Each tetrode was then examined with a microscope

to ensure smooth coating of the glue, which added both strength and insulation to the tetrodes. Examination of several 100 tetrodes made with this additional step after acute and chronic implantation showed an over 90% reduction in tip splaying. The post-coating diameter of the tetrodes was approximately 50 μm .

To estimate the location of signal sources in the tissue surrounding a tetrode, it is essential to identify accurately the four recording channels of the tetrode. Because the four wires of the tetrode are twisted together, however, the correspondence between the

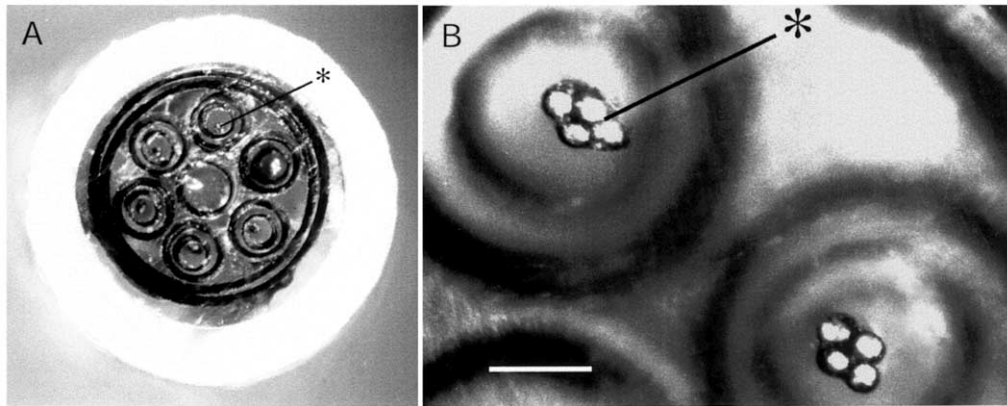


Fig. 2. Tetrode assemblies photographed from open face of the casing. (A) A 19 gauge polyimide tube glued inside a 24 gauge teflon tube holds six 30 gauge polyimide tubes through which tetrodes move. (The tip of a tetrode is indicated by asterisks.) (B) The tips of the four wires comprising a tetrode are plated with gold in order to reduce impedance. The geometric relationship of the four tips, including intra-tetrode distance, is measured during the gold plating process (see text). Scale bar in B represents 100 μm .

individual channel at the tip and at the top of the tetrode is unknown. We developed a protocol for correct assignment of channel numbers.

The machined drive assembly produces a concentric arrangement of tetrodes, individually identified as they advance out of the drive (Fig. 2). The inter-tetrode distance between tetrode 1 and each of the remaining tetrodes (5 in our example) was measured in frontal view, and the configuration of the four tips of each of the six tetrodes was drawn on a schematic diagram. The tips are then dipped in gold solution, and 0.2 μA of current was intermittently passed through only one channel (channel 1) of each tetrode, until the impedance of the channels was reduced to 200–300 $\text{k}\Omega$. Observation of the tips under the microscope identifies the plated tips as channel 1 for each of the six tetrodes, and they are marked as such on the diagram. This process is repeated to identify the tips corresponding to the remaining channels.

In order to improve the separation of clusters (see below) it was necessary to measure the impedance of the electrode tips. Daily measurements of such impedances were not carried out regularly during recording, because such measurements require current flow, which on repetition could lead to tissue damage. The electrode impedances were, however, measured throughout the development of the headstage in the rat and were found to be stable until the end of the experiments; maximum changes in the impedance occurred almost immediately after implantation. Because of this stability and the reliability of the physiological recordings over time, terminal *in vivo* measurements can be used as estimates of the impedances during the recording period.

To measure the inter-tip distances, we used a microscope with an attached digital camera and software (BIOCOM, Les Ulis, France) that allows distances between pixels of the image to be measured in the X – Y plane. The calibration on the focus dial of the

microscope was used to obtain the Z -coordinate. We calculated an average of three measurements of X , Y and Z coordinates between the tip corresponding to channel one and each of the other three tips to produce a three-dimensional coordinate system for tetrode tip geometry. Table 1 provides a representative average of 100 calibrated tetrodes. Despite a well-standardized method of tetrode manufacture, the tip-to-tip distances between the four channels of each tetrode were not constant, necessitating calibration of each individual tetrode. The calibration generates a precise coordinate system for estimating the location of signal generators in extracellular space.

3. Tetrode localization by MRI

Tetrodes can be independently moved (lowered or raised) many times over the course of an experiment. Local adjustments can be made until a brain region of interest is reached, and once recording is completed from this region, the tetrodes can be moved to record from deeper regions in the same animal. Estimates of tetrode locations *in vivo* have been entirely dependent on the accuracy of the stereotaxic coordinates and identification of known physiological characteristics of the recorded cells. *Post mortem* histological analysis identifies only the final site of recording and does not

Table 1
Average measurements for 100 tetrodes between tetrode tips with respect to tip #1^a

Channels	X – Y separation \pm S.E. (μm)	Z separation \pm S.E. (μm)
1–2	22 \pm 3	5 \pm 3
1–3	26 \pm 5	6 \pm 2
1–4	28 \pm 5	5 \pm 3

^aSignificant variability is seen in the tip–tip distance.

provide localization information in the live animal. To take advantage of the capacity for tetrodes to be used flexibly over long periods of time in chronically implanted animals, we developed an MRI protocol for in vivo tetrode localization. The drive described above was designed to have no metal parts near the skull and hence is well suited for this application. Imaging protocols were approved by the Charlestown imaging facility of the Massachusetts General Hospital.

The magnetic susceptibility of the tetrodes was determined by imaging a single tetrode suspended in a plexiglas cylinder. Individual channels of the tetrode were not visible, but the tetrode created a clear and distinct artifact 180 μm wide, establishing the imaginability of the tetrodes. To perform scans of tetrodes implanted in the brain, we constructed a plexiglas stereotaxic frame for the rat, and obtained both T1- and T2-weighted images in vivo in deeply anesthetized rats fitted with the tetrode headstage. For the tests, tetrodes were lowered to sites estimated to be in the caudoputamen. T1-weighted images allowed better separation of the artifact created by each individual tetrode than T2-weighted images, whereas T2-weighted images better defined the contrast between tissue compartments such as the neocortex, the subcortical white matter and the striatum. Subsequent superimposition of the two image sets allowed accurate measurement of the depth of each tetrode and could be used to confirm whether they had indeed entered the region of interest. The number of turns of the microdrive screw during recording and the pitch of the screw were used to estimate the depth of each tetrode, which helped to identify each tetrode visible in the MRI image.

All images were acquired in a SISCO MRI system (Varian Associates, Inc., Palo Alto, CA) equipped with a NALORAC 2.0 T (proton frequency at 84.74 MHz) 18-cm horizontal bore superconducting magnet (Martinez, CA) using a conventional 2D multislice spin-echo pulse sequence. The images were acquired with a 2 cm diameter receiver coil that is inductively coupled to a single loop 1 cm diameter transmitter coil. The coil was placed on the head of the rat around the bottom of the cone where the cone met the animal's head. The entire imaging procedure took 30–40 min and included the following steps:

- 1) The animal was deeply anesthetized (25% ketamine 100 mg/ml and 2.5% xylazine 100 mg/ml in 0.9% saline; 0.5 ml intra-peritoneally), and was secured in the plexiglas stereotaxic frame.
- 2) A multislice ($n = 7$) set of T1-weighted images was obtained in the coronal plane with the following parameters: TR = 1400 ms; TE = 20 ms; two signals acquired per phase encoding step; receiver band-

width of 10 kHz; slice thickness of 900 μm ; field of view of 3.5×3.5 cm with a resolution of 256×128 pixels.

- 3) A T1-weighted sequence with a TR/TE of 500/20 was obtained at the exact plane of the tetrodes. Typically, three to four slices in the transverse plane were acquired, with an average of 16 signals acquired per phase encoding step. The remaining parameters were the same as those for the coronal series (Fig. 3A, B and D).
- 4) If needed, T2 weighted images (TR/TE of 800/80) were collected to enhance the gray-white differentiation of the MR images (Fig. 3C and E). These images showed enhanced MR contrast between tissue compartments, but increasing the echo time of the pulse sequence also increased the magnitude of the artifact (signal loss) that was produced in the region surrounding the microelectrodes by the difference in magnetic susceptibility between the tetrodes and brain tissue. The presence of these artifacts reduced the precision in measuring the position of the tetrode in the brain, but the T2- and T1-weighted images could be compared and superimposed as needed.

The results of imaging an assembly of six tetrodes in the rat caudoputamen is shown in Fig. 3A. This imaging demonstrates the usefulness of MR imaging for tetrode localization. The coronal sections identify the A–P location of the tetrodes. By means of the subsequent transverse images obtained precisely through this location, the depth of each tetrode can be measured within a margin of error of 180 μm .

The final position of the tetrodes was assessed conventionally by making electrolytic lesions through the tetrodes. The animal was deeply anesthetized and the impedance of each channel of every tetrode was measured with an impedance meter in preparation for analysis of the recorded data (see analysis section below). Lesions were made with a Pulsar 6bp lesion maker (FHC Inc.) using single mode, bipolar stimulation (train interval 100 ms, pulse duration 500 μs). Following standard protocols, lesion locations and electrode tracts were identified microscopically in stained tissue (Fig. 3F).

4. Data analysis

4.1. Overview

The neuronal data analyzed were acquired with the interrupt-driven, spike voltage threshold-triggered data acquisition software package developed by Wilson and Frank (Frank et al., 2000). Amplified neuronal activity

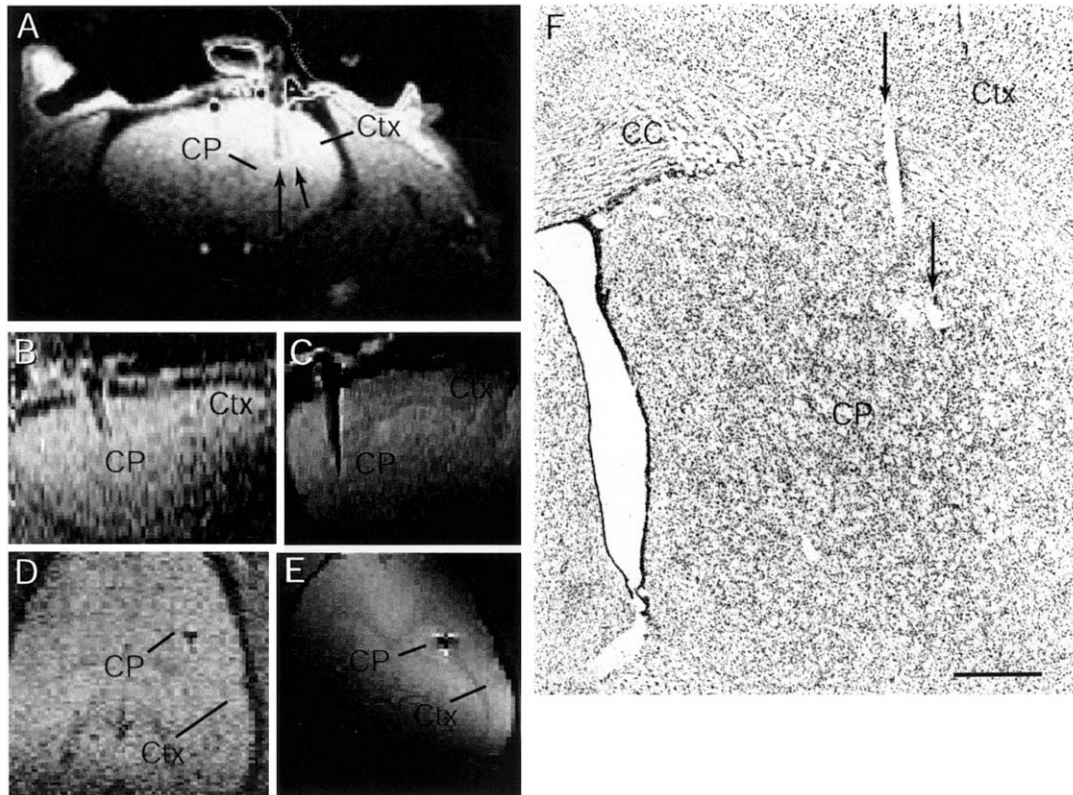


Fig. 3. In vivo and in vitro methods used to identify the location of recording sites. (A) Composite T1-weighted MRI image shows a transverse section through rat brain. On the right, tetrodes are visible, penetrating into the striatum. The darker track (long arrow) represents the image of several tetrodes; the lighter track (short arrow) indicates a single tetrode branching away from the main group. (B)–(E) show T1- and T2-weighted images of sagittal sections, and T1- and T2-weighted images of horizontal sections, respectively. Tetrode tracks are clearly visible in each image. (F) Conventional transverse section through the rat brain showing the tracks of two tetrodes (arrows) entering the dorsolateral caudoputamen (CP). Ctx, neocortex; CC, corpus callosum.

recorded by each channel (gain = 10 000, filters = 0.6–9 kHz) was digitized at 25 kHz and stored with 32 data points per spike along with a corresponding event time stamp, allowing spike waveforms to be easily reconstructed.

The data analysis package that we developed consists of a series of distinct phases. First, waveforms were classified into spike and noise events. For each spike, a power measure was computed for the waveforms on each of the four tetrode channels. This represents the spike as a point in a four-dimensional parameter space. For a given recording session, the spikes form clusters that correspond to putative neurons. With an automatic clustering algorithm on this parameter space, we labeled each spike as belonging to a putative neuron. The mean power values for each cluster were used to compute an approximate image of cell location with respect to the recording tetrode. Events (spikes) in a cluster (neuron) were then plotted as rasters against a common timebase to find common events of interest. The resulting data were then processed by conventional methods.

4.2. Signal processing

Because a tetrode has four channels, each event in its raw form consists of four sampled spike waveforms. The four tips of a tetrode are at different distances with respect to a given neuron, so that neuron's spikes will produce different waveforms on each channel. As noted by Gray et al. (1995) and Henze et al. (2000), there are large differences in signal amplitude across the four channels. This difference can be used to discriminate neurons, and can even supply an approximate map of the position of a neuron with respect to the recording tetrode. Peak amplitude can be noisy. The approach taken here to get a more robust measure of the spike's intensity is to compute a score that is a weighted average of the amplitudes near the spike peak. This is the sum of products of the waveform and the template. The waveform and the template are both in units of voltage, so that this score is proportional to spike power. The template uses all 32 captured data points, for a window duration of approximately 1.2 ms. This procedure,

described below, produces a score that can be used for discriminating waveforms and smooths the signal, reducing the effects of noise.

One major challenge in processing the recorded waveforms is eliminating EMG noise. In addition, spikes from different neuronal types (e.g. phasically active versus tonically active striatal neurons) can appear in the same session, and each type must be processed separately. The waveforms of such neurons have well identified and consistent morphologies can be used to select visually different template types corresponding to the different neurons. These templates can then be employed to screen the entire dataset, allowing spike sorting. The selection of the templates can be focused specifically to the neuron(s) of interest, thereby eliminating data from other neuronal types that are not of specific interest to the particular analysis being carried out. In this situation, only the templates that best represent the known waveform morphology of the neurons of interest need be used in the sorting of spikes.

Templates matched to the waveforms of interest were generated for each type of signal to be classified, corresponding to the signals of the medium spiny neuron or to noise. These were constructed by averaging 40 manually and visually selected waveforms, generating an idealized template for the signal type. For each incoming waveform W_k , the inner product of W_k and each template T_j was computed to produce a score b_k for channel k :

$$b_k = \sum_{i=0}^{32} W_k(t_i) T_j(t_i)$$

The sum is carried out over all 32 data points. To classify events, the sum of positive b_k values obtained for template I on the four channels was taken:

$$B = \sum_{k=0, b_k > 0}^4 b_k$$

The template that produced the highest value of B wins, and the incoming waveform was classified as belonging to the corresponding signal type. This method improves the signal purity of the dataset by reducing noise and eliminating data that are not of immediate interest, thereby serving a filtering function (Vaadia et al., 1995; Hampson and Deadwyler, 1998).

Noise events (e.g. from external electrical disturbances, or muscle) can be dealt with in two ways. Firstly, noise can be classified (and hence rejected) using templates (see below). Most noise waveforms that we encountered (> 85%) exhibited a frequency spectrum that was markedly different from the spike waveforms generated by striatal neurons. In particular, most of the

energy in these noise waveforms occurred at low frequencies. They were easily rejected using template matching.

Secondly, those noise signals that are not rejected by template matching can almost always be rejected by examining the relative power of the signal on the four tetrode channels. Noise signals generated by a strong external (infinite) source will appear with nearly identical power values on all four channels. In the four-dimensional power space, these noise events are clustered along a line passing through the origin. A straightforward test allows these noise events to be rejected.

Unique waveform templates having been generated for different neurons during spike sorting, and the data points assigned as ‘noise’ having been discarded, the remaining points are separated into distinct clusters possibly belonging to different neurons. From these remaining clusters, means and co-variances are computed for every cluster, and outlier points for every cluster are discarded based on the distance from the cluster centroid. Once the clusters have been thus ‘cleaned up’, those with the weakest power signatures are also discarded, leaving the strongest clusters for analysis (see Section 4.3 for details). Power values were computed by correlating the waveform with the matched template. The peak values of the correlogram correspond to the power signature for the signal. The following steps were taken to compute spike power signatures for each channel k of the tetrode:

- 1) Let S_k be the correlation of template T and waveform k .
- 2) Compute the first derivative of S_k (S'_k).
- 3) If $S'_k(t) = 0$ and $S_k(t) > \text{threshold } c$, then take $S_k(t)$ to be a measure of power for spike k .

In this way, each event was assigned four power measures. Let S_1 – S_4 denote the power measures obtained for one spike on each of the four tetrode channels. Each S is the sum of products of voltages, and is a measure of the amount of power of the incoming signal that can be attributed to a neuron of the appropriate type. After computation, these power measures are normalized by the measured impedances at each of the four tetrode tips, as these impedances can vary among the tips and affect the relative power measures. The four power measures then are stored along with a timestamp. By this method, each spike event is mapped to a point in a four-dimensional spike power space. Events obtained from a given recording session can be viewed as point clouds, subjected to a variety of transformations, and clustered to group events into populations with similar characteristics (Fig. 4).

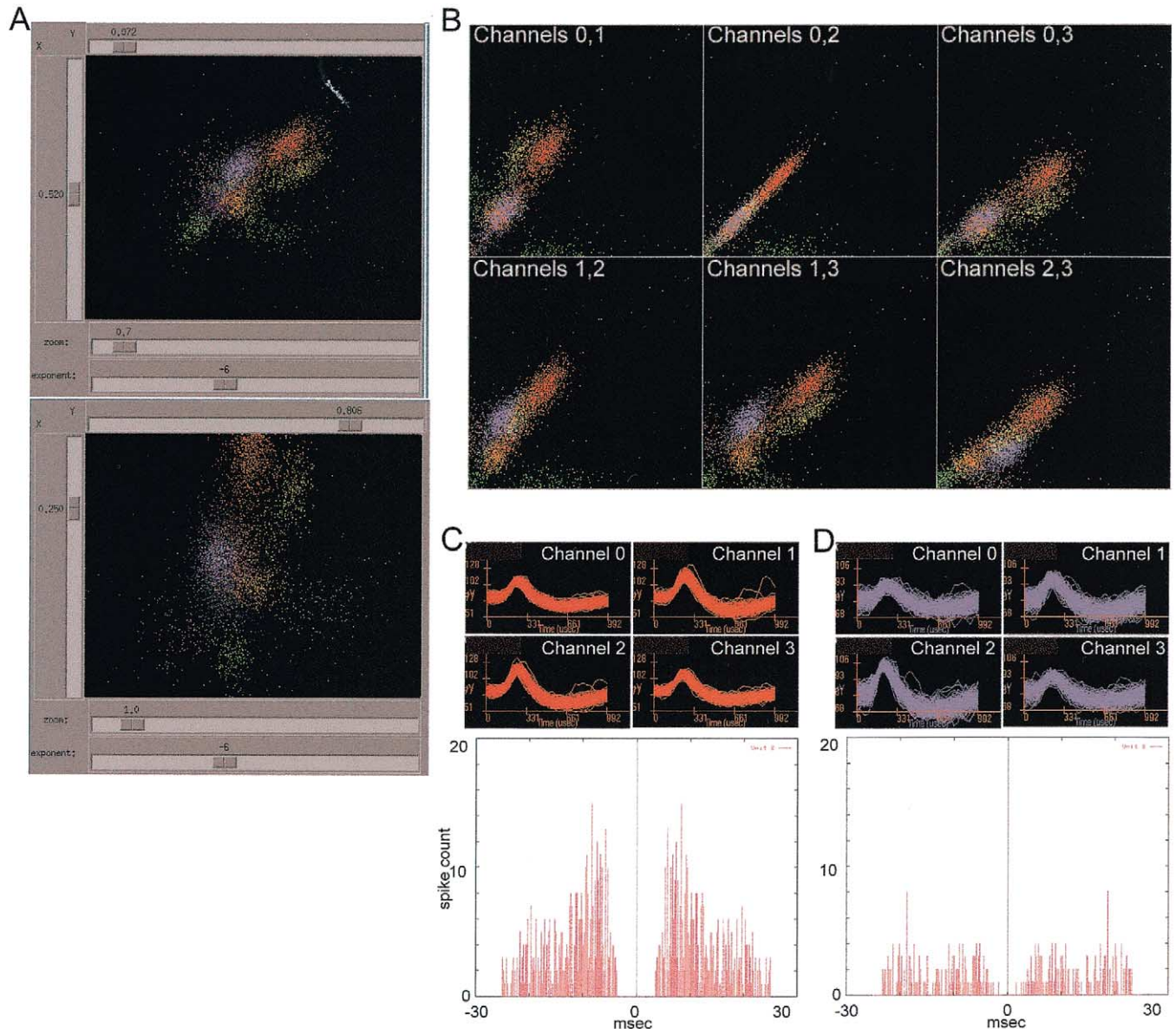


Fig. 4. Examples of cluster displays, waveform displays and inter-spike intervals plots for identified clusters. (A) Scatter dot displays of spikes (rendered as dots) calculated in three-dimensional power space representing the power measures of recordings on three of the four tetrode channels (wires) with respect to the fourth channel. Clusters of dots are color coded to indicate the spikes belonging to putative single units identified in the multi-unit activity recorded by a single tetrode. The display can be rotated to view the dot and cluster distribution at any three-dimensional angle by manipulating three scroll bars controlling the three dimensions. The two plots show displays of the same scatter plot viewed with different channels (top, channels zero, one and two; bottom, channels one, two and three) from different angles. Note that the green cluster is not separable from other dot clusters in the view shown in the top plot but is clearly separated from the other clusters in the view shown in the bottom plot. (B) Scatter dot displays of the same spikes shown in conventional two-dimensional plots using the power measures on two tetrode channels, as labeled. Note that the red and yellow clusters, which are clearly separated in the bottom three-dimensional view, are less well separated in these two-dimensional plots. (C) Spike waveforms recorded on the four tetrode channels as labeled (top) and the inter-spike interval (ISI) plot (bottom) for the red cluster shown in A and B. In the waveform displays, the horizontal axis represents time (ms), and the vertical axis represents voltage (μV). In the ISI plot, the horizontal axis represents time (ms), and the vertical axis represents spike count in 0.2 ms consecutive bins. A sorted cluster is accepted for further analysis if the proportion of spikes that occurred within a 5 ms ISI window is less than 10% of the total spikes for the cluster. About 20% of the identified clusters did not meet this criterion, and were discarded from the data analysis. (D) Spike waveform displays and the ISI plot for the purple cluster shown in A and B.

4.3. Spike sorting

Manual spike sorting is subjective and subject to error (Gray et al., 1995; Henze et al., 2000). In an effort to alleviate this problem, we developed an unsupervised spike sorting algorithm for grouping spike events into distinct clusters. This method provides an initial, objective partitioning of the data. It is common practice for tetrode clustering systems to display many two-dimensional orthographic projections of the parameter space (Fig. 4B). Fixed orthographic projections, however, can lead to cluster occlusion. That is, there are configurations of clusters that can cause one cluster to be hidden behind others in all six views of the data set. To avoid this problem, we developed a display that allows three-dimensional cluster plots with perspective and stereo that can be rotated along any dimension (Fig. 4A). This combination of unsupervised classification and examination of the parameter space reduces the subjectivity involved in cluster separation while at the same time maximizing the value of user interaction in the clustering process.

To separate recorded events into groups corresponding to putative neurons, the events are plotted and clustered in the four-dimensional power-signature space. Each event is a single point in this space. Clustering is implemented using the K-Means algorithm (Duda and Hart, 1973). The user can select three out of the four dimensions to be plotted. The plots can be viewed and rotated in three dimensions at a time, so that the point set and clusters can be examined and edited if necessary.

The K-Means algorithm assumes that k clusters have been chosen, and that each point has been assigned to one of these clusters. As it was rare to see more than eight clear clusters in our data, k was chosen to be somewhat larger than this (usually 12). Clusters are computed by first spreading k random seed points to generate a number of initial clusters. Points are then moved between clusters only if they reduce the global clustering error E :

$$E = \sum_{i=1}^k \sum_{p \in S_k} \|p - \mu_k\| \quad (1)$$

where S_k is the set of points in cluster k , and μ_k is the mean (centroid) for cluster k . When no more points can be moved in this fashion, clustering is terminated. Finally, these clusters are visually reviewed to determine whether they represent a satisfactory clustering of the data. Scatter matrices for the clusters are also computed at this stage. The most distant points (corresponding to the weakest signals) tend to be over-clustered. It is difficult to resolve these weak signals into clear clusters, and they could be discarded when analyzing experimental data. However, users can also request waveform plots displays and inter-spike intervals for individual

clusters to help assess cluster quality (Fig. 4C and D). The display is three-dimensional, so that users have the option of choosing any three out of the four dimensions (Fig. 4A). In addition, side-by-side three dimensional rotating scatter plots allow all relevant dimensions to be displayed simultaneously, allowing the user a full view of all dimensions of the cluster parameter space. This helps the user to avoid the hidden cluster problem.

These scatter matrices approximate the covariances of events in each cluster and describe the possibly elongated shape of the clusters. The distance measure used in Eq. (1) above is actually a Mahalanobis distance (Duda and Hart, 1973), in which covariance is the metric, i.e. if C is a covariance matrix, then the corresponding Mahalanobis distance is:

$$\|p - \mu_k\| = [p - \mu_k]^T C [p - \mu_k] \quad (2)$$

If the clusters are not satisfactory, a new number of seed points can be used, and the process repeated. Global clustering error can be used to determine whether such a reclustering is warranted. If desired, the user can edit the automatically produced clusters either by thresholding the Mahalanobis distance to reject outliers, or by explicitly selecting groups of points to be added or deleted. When rejecting outliers by distance, the user can choose a threshold distance as measured by Eq. (2), or choose a threshold as a fraction of the total mass of the corresponding Gaussian distribution. Either method is accessible as a slider control in the user interface.

After clustering, we assessed the quality of correlation-based vs. amplitude-based scoring by comparing the compactness of clusters with respect to the corresponding full dataset. For each dataset, covariance (scatter) matrices were computed for each cluster and for the entire dataset, using both amplitude-based and correlation-based scores. Cluster compactness was measured by computing the ratio of the determinant of the cluster covariance matrix and the determinant of the entire dataset's covariance matrix. The determinant of a covariance matrix is the volume of the ellipsoid corresponding to one standard deviation. The ratio of determinants therefore expresses the volume of one cluster relative to the entire dataset. By this measure, correlation-based scores resulted in more compact clusters than amplitude-based scores 74% of the time. On average, correlation-based power measures reduced relative cluster volume by 8% over amplitude-based measures. This demonstrates the utility of a correlation-based scheme, which is borne out by a more compact visual display of clusters.

4.4. Triangulation

To obtain a position image for neurons recorded on a given tetrode, certain specific assumptions are made: (1)

Each action potential (spike) produces an approximately spherical wavefront (Halliday and Resnick, 1962). (2) Attenuation in extracellular space is constant over time. (3) The power output for a given cell is constant. (4) Each tetrode has four tips labeled 0, 1, 2, 3, 5. Tip 0 is at the origin.

Our analysis is greatly simplified by the assumption that the neurons analyzed exhibit a relatively constant power output. This lets one assume that the neuron is effectively a point source for the spike, and that the resulting impulse travels as a roughly spherical wave through the nearby tissue.

Under these assumptions, voltages propagate according to an inverse- r law. If one considers propagation of an ‘infinitely distant current source’ relative to the cell soma, by Rall’s analysis (Rall, 1962) the following relationship holds among (extracellular) voltage, V_e , current I_e , resistivity R_e , and radius r from the soma:

$$V_e = \int_r^{\infty} \frac{I_e R_e}{4\pi\rho^2} d\rho$$

Integrating this equation under a constant-current assumption yields:

$$V_e = \frac{-I_e R}{4\pi r}$$

As a result, voltage is inversely proportional to distance from the soma. This prediction is consistent with the voltage–distance plots presented by Henze et al. (2000). One can view this process in terms of the intensity of spherically propagating waves, which decrease in proportion to the density of the wavefront, the area of which is increasing as the inverse square of distance from the wave source. The spherical wave assumption is also in general agreement with Rall’s original results, when distance to the soma is short (e.g. a 60–80 μm radius), as in the case of tetrode recordings.

In contrast to the inverse- r law for voltage, the intensity I of the spike, as recorded at one tip of the tetrode, is related to the inverse square of the distance from neuron to tip (Halliday and Resnick, 1962):

$$P = 4\pi r^2 I$$

where r is the neuron-tip distance, and P is the power output of the neuron’s action potential at the source. The spike wavefront intensity I is assumed to be proportional to event power measures $S = aI$, where the constant a represents signal attenuation arising from other factors (e.g. impedance). The inverse square law can be rewritten as:

$$\frac{c}{S} = \frac{aP}{4\pi S} = r^2 = x^2 + y^2 + z^2$$

As the spike is assumed to propagate as a spherical

wave, a system of equations corresponding to a set of four intersecting spheres can be written. This system can be used to solve for the spike position x in terms of the channel tip positions x_i . To simplify the calculation, one channel is assumed to be at the origin:

$$\frac{c}{S_0} = x^2 + y^2 + z^2 \quad (3)$$

whereas the others are offset by $x_n; y_n; z_n$:

$$\frac{c}{S_1} = (x - x_1)^2 + (y - y_1)^2 + (z - z_1)^2$$

$$\frac{c}{S_2} = (x - x_2)^2 + (y - y_2)^2 + (z - z_2)^2$$

$$\frac{c}{S_3} = (x - x_3)^2 + (y - y_3)^2 + (z - z_3)^2$$

$$\frac{c}{S_0} = (x - x_1)^2 + (y - y_1)^2 + (z - z_1)^2$$

The x^2, y^2, z^2 terms can be eliminated by subtracting each equation above from Eq. (3). Letting $\Delta_n = x_n^2 + y_n^2 + z_n^2$ this yields:

$$c \left(\frac{1}{S_0} - \frac{1}{S_1} \right) = 2xx_1 + 2yy_1 + 2zz_1 - \Delta_1 \quad (4)$$

$$c \left(\frac{1}{S_0} - \frac{1}{S_2} \right) = 2xx_2 + 2yy_2 + 2zz_2 - \Delta_2 \quad (5)$$

$$c \left(\frac{1}{S_0} - \frac{1}{S_3} \right) = 2xx_3 + 2yy_3 + 2zz_3 - \Delta_3 \quad (6)$$

Defining the following:

$$A = \begin{bmatrix} x_1 & y_1 & z_1 \\ x_2 & y_2 & z_2 \\ x_3 & y_3 & z_3 \end{bmatrix}$$

$$p = \begin{bmatrix} \frac{1}{S_0} - \frac{1}{S_1} \\ \frac{1}{S_0} - \frac{1}{S_2} \\ \frac{1}{S_0} - \frac{1}{S_3} \end{bmatrix}$$

the system can be rewritten in matrix form as:

$$cp = 2Ax - \Delta \quad (7)$$

Note that the matrix A has a clear geometric meaning: it is simply the matrix of positions of tips 1–3 relative to tip 0. If the tetrode tips are not all colinear or coplanar, then the matrix A is invertible. This underscores the importance of tip geometry in tetrode fabrication: to get maximum cluster separation, one should insure that the tetrode tips are as evenly separated as possible in all three dimensions. In other

words, the eigenvalues of A should all be non-zero and nearly equal. If the tips are indeed coplanar, then the cluster space becomes three-, not four-dimensional. Reduction of dimension reduces cluster separability and may cause some clusters to be merged.

Rearranging terms in Eq. (7) then yields:

$$x = \frac{1}{2} A^{-1}(cp + \Delta)$$

$$x = \frac{cA^{-1}p + A^{-1}\Delta}{2}$$

This equation describes a solution ray, parameterized by c , in the three-dimensional space surrounding the tetrode. We can solve for c by substituting x into Eq. (3):

$$\frac{c}{S_0} = \frac{1}{4} \|cA^{-1}p + A^{-1}\Delta\| \quad (8)$$

The result is a ray piercing a sphere, as shown in Fig. 5. For the two roots of Eq. (8), c must be positive to be physically meaningful, so only the positive root is used for reconstruction.

The spatial maps that result from this reconstruction technique show that, in general, active neurons are a relatively sparse subset of the surrounding neuropil in the test tissue, the rat striatum. We base this observation on the fact that striatal tissue consists of medium spiny neurons that are tightly packed within the tissue. Our reconstructions show that active cells are typically several soma diameters apart (i.e. on the order of 20–

50 μm apart). The upper limit for resolvable clusters is generally between 80 and 100 μm as determined by our reconstructions. This range is similar to that found by Harris et al. (2000) for the hippocampus.

Our analysis uses a simple model for signal propagation through extracellular space. In particular, the measured intensity S is subject to bandpass filtering and attenuation that may introduce error into the computation. Nonetheless, we note that the distance measurements made by Harris et al. (2000) in the hippocampus are consistent with the theoretical analysis presented here. These measurements are also consistent with our observations that the spike activity of individual cells could be monitored through a 200 μm traversal of tissue (a pickup radius of approximately 100 μm). Henze et al. (2000) compared intracellular and extracellular tetrode recordings, and from this suggest that, in the hippocampus, only a small portion of the cells near the tetrode are active at any time. Our observations support that the same may be true in the striatum.

5. Discussion

Simultaneous recording and analysis of the activity of large numbers of neurons during natural behaviors is a crucial tool for neuroscience. Tetrode technology has significantly advanced the field by permitting recording of neuronal ensemble activity with high level of accuracy in identification of individual neurons (Recce and O'Keefe, 1989; Wilson and McNaughton, 1993; Gray et al., 1995; Harris et al., 2000; Henze et al., 2000). We report here developments in tetrode technology and in methods of analysis of data acquired by recording with tetrodes in freely moving rodents. Hardware developments include the design and fabrication of a reusable precision-machined almost entirely plastic drive assembly and modifications in the tetrode manufacture process. These non-magnetic drives allow tetrodes to be imaged in vivo by MRI. We also describe a data analysis technique that includes three dimensional display, unsupervised cluster separation with user modifiability and estimation of the signal source location. The capacity to estimate putative signal source location and the temporal analysis capability of the software allow a detailed examination of the relationships among units that are close (recorded on a single tetrode with identified locations of each recording channel) and among units that are relatively far away from each other (recorded on separate tetrodes).

Our analysis has not dealt with sources of misclassification of data such as spike overlap and signal drift. Spike overlap (the occurrence of multiple spikes within a capture window) requires special analysis. In the striatum, in which most neurons fire at low rates, spike

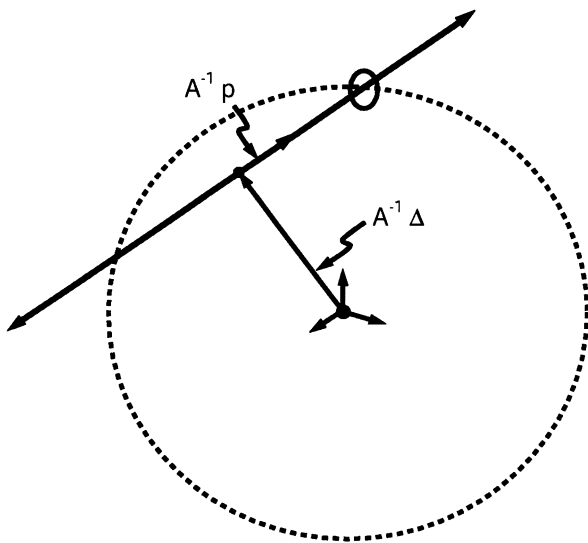


Fig. 5. This diagram illustrates neuronal localization in the Cartesian coordinate system around the tetrode, where the origin is at tip 1. The triangulation algorithm computes the intersection of the ray (bold line) within a sphere (dotted circle) in terms of a parameter c common to both the ray and the sphere. The small circle near the top right represents the physically valid solution corresponding to $c > 0$.

overlap should be relatively rare. When overlap does occur, multiple peaks can be isolated by localizing the zero-crossing of the first derivative of the waveform, and accepting signal peaks that meet a threshold criterion. It may be possible to use model-based methods to decompose these overlapping spikes into individual waveforms, if enough is known about the typical waveforms of the neurons.

A major source of drift is tissue movement occurring after the electrode is advanced, and this can usually be minimized by waiting periods after electrode advancement during which the stability of the recording is monitored. Other sources of drift, such as respiration-induced changes in brain volume, are more difficult to compensate. In our datasets, this source of drift was noticeable, but did not interfere with our ability to identify clusters reliably. Current methods for detecting drift include computing a moving average to describe the change in cluster centroids over the course of a session. An alternate method would be to perform a similar analysis over the entire dataset, but this method would not be robust with respect to spontaneous activation of new units.

An active interface between multi-neuronal recording and functional neuroimaging holds clear potential (Logothetis et al., 2001). The non-magnetic drives described here, which allow tetrodes to be imaged in vivo by MRI, should extend this interface to small animals, favored species for genetic manipulation.

Acknowledgements

This work was supported by NIMH RO1-MH60379, NINDS P50-NS38372 and NIMH RO3-MH57878; the Medical Research Council of Canada, Royal College of Physicians and Surgeons of Canada; and SRI International, Menlo Park.

References

Deadwyler S.A., Hampson R.E.. The significance of neural ensemble codes during behavior and cognition. *Annu Rev Neurosci* 1997;20:217–44.

- Duda R., Hart P.. *Pattern Classification and Scene Analysis*. New York: Wiley, 1973.
- Eichenbaum H.B., Davis J.L.. *Neuronal Ensembles: Strategies for Recording and Decoding*. New York: Wiley-Liss, 1998.
- Frank L.M., Brown E.N., Wilson M.. Trajectory encoding in the hippocampus and entorhinal cortex. *Neuron* 2000;27:169–178.
- Gray C.M., Maldonado P.E., Wilson M., McNaughton B.L.. Tetrodes markedly improve the reliability and yield of multiple single-unit isolation from multi-unit recordings in cat striate cortex. *J Neurosci Methods* 1995;63:43–54.
- Halliday D, Resnick R, Physics. New York: John Wiley & Sons, 1962.
- Hampson R.E., Deadwyler S.A.. Methods, results, and issues related to recording neural ensembles. In: Eichenbaum H.B., Davis J.L., editors. *Neuronal Ensembles: Strategies for Recording and Decoding*. New York: Wiley, 1998:207–34.
- Hampson R.E., Deadwyler S.A.. Pitfalls and problems in the analysis of neuronal ensemble recordings during behavioral tasks. In: Nicolelis M.A.L., editor. *Methods for Neural Ensemble Recordings*. Boca Raton: CRC Press, 1999:229–48.
- Harris K.D., Henze D.A., Csicsvari J., Hirase H., Buzsáki G.. Accuracy of tetrode spike separation as determined by simultaneous intracellular and extracellular measurements. *J Neurophysiol* 2000;84:401–14.
- Henze D.A., Borhegyi Z., Csicsvari J., Mamiya A., Harris K.D., Buzsáki G.. Intracellular features predicted by extracellular recordings in the hippocampus in vivo. *J Neurophysiol* 2000;84:390–400.
- Jog M., Kubota Y., Connolly C.I., Hillegaart V., Graybiel A.M.. Building neural representations of habits. *Science* 1999;286:1745–9.
- Kubota Y., Hu D., DeCoteau W.E., Harlan R., Graybiel A.M.. Multi-neuronal activity in mouse striatum recorded chronically during T-maze learning. *Soc Neurosci Abstr* 2000;26:683.
- Kubota Y., Jog M.S., Connolly C., Graybiel A.M.. Cross-correlational analysis of neuronal activity in the rat striatum during T-maze procedural learning. *Soc Neurosci Abstr* 1999;25:1384.
- Logothetis N.K., Pauls J., Augath M., Trinath T., Oeltermann A.. Neurophysiological investigation of the basis of the fMRI signal. *Nature* 2001;412:150–7.
- Rall W.. Electrophysiology of a dendritic neuron model. *Biophys J* 1962;2:145–67.
- Reece M., O'Keefe J.. The tetrode: a new technique for multi-unit extracellular recording. *Soc Neurosci Abstr* 1989;15:1250.
- Skaggs W.E., McNaughton B.L.. Replay of neuronal firing sequences in rat hippocampus during sleep following spatial experience. *Science* 1996;271:1870–3.
- Vaadia E., Haalman I., Abeles M., Bergman H., Prut Y., Slovin H., Aertsen A.. Dynamics of neuronal interactions in monkey cortex in relation to behavioural events. *Nature* 1995;373:515–8.
- Wilson M.A., McNaughton B.L.. Dynamics of the hippocampal ensemble code for space. *Science* 1993;261:1055–8.
- Wilson M.A., McNaughton B.L.. Reactivation of hippocampal ensemble memories during sleep. *Science* 1994;265:676–9.